Repository of the Max Delbrück Center for Molecular Medicine (MDC) in the Helmholtz Association

ERK1 as a therapeutic target for dendritic cell vaccination against high-grade gliomas

Ku, M.C. and Edes, I. and Bendix, I. and Pohlmann, A. and Waiczies, H. and Prozorovski, T. and Guenter, M. and Martin, C. and Pages, G. and Wolf, S.A. and Kettenmann, H. and Uckert, W. and Niendorf, T. and Waiczies, S.

ERK1 as a Therapeutic Target for

Dendritic Cell Vaccination against High-Grade Gliomas

Min-Chi Ku,[1] Inan Edes,[2] Ivo Bendix,[4] Andreas Pohlmann,[1] Helmar Waiczies,[5] Tim Prozorovski,[6] Martin Günter,[1] Conrad Martin,[5] Gilles Pagès,[7] Susanne A. Wolf,[3] Helmut Kettenmann,[3] Wolfgang Uckert,[2] Thoralf Niendorf,[1] and Sonia Waiczies[1]*

[1] Berlin Ultrahigh Field Facility (B.U.F.F.), [2] Molecular Cell Biology and Gene Therapy, and

[3] Cellular Neurosciences, Max Delbrück Center for Molecular Medicine (MDC), Berlin, Germany

[4] Department of Pediatrics I, Neonatology, Universitätsklinikum Essen, Essen, Germany

[5] MRI TOOLs GmbH, Berlin, Germany

[6] Department of Neurology, Heinrich Heine University, Düsseldorf, Germany

[7] University Nice-Sophia Antipolis, Institute for Research on Cancer and Aging of Nice, Nice, France

Corresponding author: Dr. Sonia Waiczies, B.U.F.F., MDC, Robert Rössle Str. 10, 13125 Berlin, Germany

℡: +49 30 94064542; 🖷: +49 30 94064517; email: sonia.waiczies@mdc-berlin.de

Running title: Targeting ERK1 in DC Vaccines for Glioma

Keywords: ERK1, high grade glioma, dendritic cells, cell migration, and ^{19}F MRI

Potential conflict of interest: S.W. received research grants from Novartis for a different project. H.W. is employed by and T.N. is founder of MRI.TOOLS GmbH. No potential conflicts of interest were disclosed by the other authors.

Word count: 5423

Total number of figures: 7

Abstract

Glioma regression requires the recruitment of potent anti-tumor immune cells into the tumor microenvironment. Dendritic cells (DCs) play a role in immune responses to these tumors. The fact that DC vaccines do not effectively combat high-grade gliomas, however, suggests that DCs need to be genetically modified especially to promote their migration to tumor relevant sites. Previously, we identified extracellular signal-regulated kinase (ERK1) as a regulator of DC immunogenicity and brain autoimmunity. In the present study, we made use of modern magnetic resonance methods to study the role of ERK1 in regulating DC migration and tumor progression in a model of high-grade glioma. We found that ERK1-deficient mice are more resistant to the development of gliomas, and tumor growth in these mice is accompanied by a higher infiltration of leukocytes. ERK1-deficient DCs exhibit an increase in migration that is associated with sustained Cdc42 activation and increased expression of actin-associated cytoskeleton-organizing proteins. We also demonstrated that ERK1 deletion potentiates DC vaccination and provides a survival advantage in high-grade gliomas. Considering the therapeutic significance of these results, we propose ERK1-deleted DC vaccines as an additional means of eradicating resilient tumor cells and preventing tumor recurrence.

Introduction

High-grade gliomas, particularly glioblastoma multiforme (GBM), remain the least curable tumors with a high rate of recurrence and low survival rates (1). GBM evade elimination in many ways, particularly by promoting complex neovascularization networks (2) and prohibiting anti-tumor immunological surveillance (3). Therapeutic strategies will likely need to target these features from many possible angles to successfully eliminate tumors and prevent their recurrence. Feasible approaches include restoring, promoting and maintaining natural anti-tumor immune responses through immune cell therapies such as dendritic cell (DC) vaccines (4).

DCs are potent antigen-presenting cells that have been shown to initiate adaptive immune responses. DC-based immunotherapies are being pursued as potential tools in curing GBM. DCs loaded with patient-derived tumor antigens have been investigated in early clinical trials that have yielded a therapeutic proof-of-principle (5). However, multiple phase III trials have not yet demonstrated a clear superiority of DC vaccination over standard chemotherapy, even though they have prolonged the median and overall survival rate of patients (4). Taking advantage of the full therapeutic potential of DC vaccines will require a better understanding of their role in eliminating tumor tissue. A major limiting factor in DC vaccinations is the small proportion of DCs (fewer than 5 %) that reach draining lymph nodes (LNs) following administration (6). This might hamper their therapeutic efficacy. Non-invasive methods such as MRI are therefore necessary to study DC migration as measure of therapy outcome and might help identify strategies overcoming the poor DC migration observed in patients (6).

ERK MAP kinases have been shown to control cell migration by regulating cytoskeletal and focal contact dynamics (7). In myeloid DCs, persistent ERK activation leads to a

3

reduced migration of DCs, while ERK inhibition is associated with a higher migratory phenotype (8). Notably, ERK activation prevented immune cell infiltration in the articular capsule in autoimmune arthritis (9). Most studies have validated the role of ERK1 in combination with ERK2; it is however becoming clearer that these isoforms have explicitly different functions (10). When we specifically studied ERK1 in a model of neuroinflammation using bone marrow chimeras, we observed an increased infiltration of CD11c^{+} cells close to inflamed areas in the brain (11). ERK1 thus appears to be an important regulator of DC immunogenicity and its absence precipitates severe brain autoimmunity (11).

Taking these findings into consideration, we hypothesized that ERK1 is an important regulator of DC migration and that its deletion might increase the migratory properties and vaccination efficacy of DCs towards high-grade gliomas. We used high resolution proton (^{1}H) and fluorine (^{19}F) MR methods to study the role of ERK1 in tumor progression as well as DC migration. ERK1-deficient mice were more resistant to the development of WT gliomas, and their tumors were highly infiltrated with Fascin^{+} and CD11c^{+} cells. We observed a marked increase in the *in vitro* and *in vivo* migration of *Erk1*^{-/-} bone marrow derived DCs (BMDC). We also showed a marked reduction in tumor size and increase in survival following treatment of WT GBM mice with *Erk1*^{-/-} DC, which suggests ERK1 deletion in DC vaccines as additional therapeutic strategy against high-grade gliomas.

4

Materials and methods

Preparation of retroviral vectors and transduction of murine cells

The production of retroviral vectors MP71-OVA-IRES-GFP and the transduction of GL261 cells and murine T cells are presented in Supplementary Methods.

Mice and glioma animal model

All mice were handled according to the Berlin State review board at the Landesamt für Gesundheit und Soziales (LAGeSo) and internal (MDC) rules and regulations. The following mice were used: *Erk1$^{-/-}$* mice on C57BL/6 background (12), their wild-type litermates, and Rag1$^{-/-}$/OTI TCR transgenic mice recognizing the OVA-derived cognate peptide SIINFEKL on H2kb. *Erk1$^{+/+}$ × tdRFP* and *Erk1$^{-/-}$ × tdRFP* mice were generated by intercrossing *Erk1$^{-/-}$* knockout mice (12) to *ROSA26^{tdRFP}* reporter mice (13) and the F1 generation. Following anesthesia and using stereotactic (David Kopf Instruments) coordinates referenced from bregma, glioma cells (2×10^4 cells in 1-µl) were implanted in the striatum (anteroposterior 1mm; mediolateral ±1.5 mm; dorsoventral −4 mm).

Dendritic cells

Mouse dendritic cells were prepared from adult C57BL/6 mice as described (11). Briefly, BMDC were generated from femurs of WT or *Erk1$^{-/-}$* mice. Cells were grown in RPMI 1640 medium supplemented with 10% FCS and 30ng/mL GM-CSF (eBioscience). Cells were replenished with fresh GM-CSF medium every 3 days. On day 9, the fully differentiated BMDC were ready for further experiments.

In vitro migration assays

Murine CD4^{+} T cells were sorted and activated with anti-CD3/anti-CD28 antibodies for 72 h. For both murine BMDC and T cells, 600 µl of RPMI 1640 with or without recombinant stromal-derived factor CXCL12 (125 ng/ml, R&D Systems) was added to 24-well plates (lower chamber). In some case, MEK inhibitor U0126 at 10 µM was applied 30 min prior to the assay. 100 µl of cell suspension (2×10^5) was added to an upper chamber consisting of a transwell polycarbonate insert with 5-µm pore size (6.5 mm diameter; Costar Corning). The cells were then allowed to migrate at 37 °C for 3 h. Cells in the lower chamber were then collected and counted by flow cytometry.

Another method involved an agarose spot assay (14). Briefly, agarose spots with or without 2 µg/ml CCL19 (Peprotech) were placed onto 35-mm glass dishes (MatTek) and BMDC were added for 3 h. The migration of BMDC under the spots were determined by acquiring and fusing the microscope images for all the fields of views (FOV). Image processing and analysis were done with Fiji (Image J v1.47p).

Flow cytometry

TIL single cell suspensions (5×10^5) were stained for 25 min at 4 °C with fluorescently conjugated antibodies in FACS buffer after blocking low affinity Fcγ receptor with CD16/CD32 antibody (BD Bioscience). The following antibodies were from Biolegend: APC-anti–mouse CD3 (clone: 145-2C11), PE-Cy7-anti–mouse CD11c (clone: N418), Pacific blue-anti–mouse CD8a (clone: RM4-5). For fascin1 (antibodies-online Inc.) staining, cells were fixed 10 mins with 4 % PFA then permeabilized 30 mins with methanol. Cytometry acquisition was on an LSRFortessa™ cell analyzer (BD) and analysis was done using FlowJo (Tree Star).

6

Cdc42 GTP loading and immunoblotting

BMDC were treated with CXCL12 (100ng/ml) for 1 min and Cdc42 GTPase activity determined using a pull down and detection kit (Thermo Scientific). Total lysate (20µg protein) was incubated with a GST fusion protein, and then analyzed by 12% SDS-PAGE and immunoblotting according to the manufacturer's instructions. Guanosine 5'-O-[γ-thio] triphosphate (GTPγS) nucleotide was used as positive control. Membranes were incubated with secondary antibody and detected as previously described (15).

MRI methods

All *in vivo* MR measurements were performed on a 9.4 Tesla small animal MR system (Biospec 94/20, Bruker Biospin). Mice were anesthetized by inhalation narcosis using 0.5 - 1.5% isoflurane (Baxter), pressurized air and oxygen. Core body temperature was maintained at 37°C. Respiration rate and temperature were monitored using a remote monitoring system (Model 1025, SA Instruments Inc.). For further details on MR methods, please refer to Supplementary Methods.

Isolation and analysis of immune cells from glioma tissue

Tumor infiltrating leukocytes (TILs) were isolated as described (16). TILs obtained from 3 mice were pooled due to the limited cell number. Briefly, mice were transcardially perfused with PBS. Brain tumor tissue was extracted and mechanically dissociated using glass potter homogenizers (model TT57.1 Roth) into a crude suspension in RPMI 1640 complete media followed by filtering with 40-µm cell strainer (BD Falcon). Cell suspensions were spun on Percoll gradient, centrifuged at 800g for 20 min, collected from the cell interface and washed 2 times with FACS buffer. For FACS analysis, please refer to Supplementary Methods.

7

Immunofluorescence microcopy

Mouse brains for sectioning were prepared as described (14). Sixteen μm thick brain sections were mounted on glass slides. After blocking, primary antibodies were added overnight at a dilution of 1:50 for CD11c or 1:25 for CD8a (BD Pharmingen) at 4°C. Alexa 488-conjugated goat anti-guanine pig IgG (Invitrogen) or Rhodamine Red™-X (Jackson ImmunoResearch) was subsequently applied. All images were taken using a confocal microscope (LSM 710, Zeiss) with a 20× objective.

For detecting f-actin in BMDC, 1.5×10^5 cells were plated on 1mg/ml poly-D-lysine (Sigma-Aldrich) coated glass cover slips. Cells were fixed with 4% PFA, and stained with rhodamine-coupled phalloidin (1:50; Molecular Probes®, Invitrogen). Images were taken by inverse fluorescence microscope (Leica) and digitized by Leica DC Viewer 3.2. For detecting fascin1 in BMDC, 2×10^4 cells were plated on glass cover slips. Fixed cells were permeabilized with 0.01% Triton X100. The nuclei were counterstained with Hoechst 33342 (1:1000, Sigma-Aldrich). Images were taken using a confocal microscope (LSM 710 Zeiss) with a 40× objective.

Quantification of CD8$^+$ tumor infiltrating T cells

Immunofluorescent staining sections from two animals of each group (PBS, WT-DC, and *Erk1*$^{-/-}$ DC treated) of glioma-bearing mice were used for quantification of CD8$^+$ tumor infiltrating T cells. For each section, CD8$^+$ T cells from at least 5 random fields within the tumor region were counted, each field measuring 1-2mm^2. Cell number from each group were normalized with tumor area. Cell quantification was performed with Fiji (Image J v1.47p).

BMDC-T cell coculture and ELISA

BMDC from WT and *Erk1*$^{-/-}$ mice (5×10^4), preloaded with either SIINFEKL (1μg/ml, Biosynthan), full-length EndoGrade ovalbumin protein (1μg/ml; Hyglos) or OVA-GL261 cell lysate (50μg protein/ml), were cocultured with 5×10^4 OT1-TCR-transduced T cells (OT1-T cell). PMA (20ng/ml) and ionomycin (1μg/ml) were used for positive controls. IFN-g concentration in was determined 24 h later by enzyme-linked immunosorbent assay (BD Bioscience).

DC vaccination protocol

BMDC from WT and *Erk1*$^{-/-}$ mice were incubated with GL261 cell lysate (50 μg protein /ml) and after 3 h, DCs were further matured with 0.5μg/ml LPS and incubate for 18 h. On day 3, 7, 10, and 14 following tumor implantation, WT mice were divided into 3 groups and treated by intraperitoneal (i.p.) injections of either PBS or 2×10^6 BMDC (WT BMDC, n=10; *Erk1*$^{-/-}$ BMDC, n=10; PBS, n=10). Survival studies were performed between different groups and the survival rate was calculated by the Kaplan-Meier method (MedCalc) using log-rank analysis.

Statistical group analysis

All data represent the average of at least triplicate samples. Error bars represent standard error of the mean (SEM). All data are presented as mean±SEM. Data were analyzed by Student's t test when compared between 2 groups. When comparing more than 2 groups, one way ANOVA was used in Microsoft Office Excel 2010. For multiple comparisons the Bonferroni correction was applied. Kaplan-Meier method was used for survival rate using log-rank analysis. The differences were considered statistically significant at *$p<0.05$, **$p<0.01$, and ***$p<0.001$.

9

Results

Glioma growth is diminished in ERK1-deficient mice

The role of ERK1 in the glioma tumor microenvironment or its indirect impact on tumor progression is unknown. We stereotactically implanted WT GL261 glioma cells in the striatum of either WT or ERK1-deficient (*Erk1$^{-/-}$*) mice. Using a previously established, high spatial resolution MRI protocol (14), we observed a marked reduction in glioma tumor growth in *Erk1$^{-/-}$* compared to WT mouse brains 14 days post implantation (dpi) (Fig. 1A, left panel). Tumor volume was significantly smaller in *Erk1$^{-/-}$* mice (9.6±1.1 mm^3) compared to WT mice (18.6±2.1 mm^3) (Fig. 1A, right panel, p=0.00172). The survival rate in *Erk1$^{-/-}$* glioma-bearing mice was also markedly improved compared to WT glioma mice (Fig. 1B, p=0.0002). Notably, two out of eleven *Erk1$^{-/-}$* glioma-bearing mice exhibited complete tumor rejection. Altogether, these data indicate that the deletion of ERK1 in the stroma significantly attenuates glioma progression.

Glioma-induced immune cell infiltration is regulated by ERK1

High-grade gliomas contain brain-infiltrating peripheral immune cells among other cell types (17). We employed a ^{19}F MR method (18) to study the way leukocytes leave the circulatory system and infiltrate the tumor site in WT and *Erk1$^{-/-}$* mice harboring WT gliomas. Prior to ^{19}F/^{1}H MRI, rhodamine-^{19}F nanoparticles (19) were i.v. injected into WT and *Erk1$^{-/-}$* glioma-bearing mice (18 dpi) to label leukocytes traveling within the blood circulation (Fig. 2A). These cells take up nanoparticles, migrate into the brain, infiltrate glioma tissue (tumor-infiltrating leukocytes or TILs) and can then be visualized using ^{19}F MRI. Upon segmentation of the whole tumor region, we calculated a 1.7-fold increase of total ^{19}F signal within tumors in *Erk1$^{-/-}$* mice compared to WT. Considering

the significantly smaller size of these tumors in the *Erk1*$^{-/-}$ mice, we next calculated the ^{19}F signal per tumor volume, which reflects the density of ^{19}F-labeled TILs within the tumor and observed a 2.4-fold (p=0.0098) increase in *Erk1*$^{-/-}$ versus WT glioma-bearing mice (Fig. 2B, right panel). *Ex vivo* immunofluorescence staining also revealed that higher numbers of CD11c^{+}/^{19}F rhodamine-labeled cells infiltrated the tumor region in *Erk1*$^{-/-}$ brain sections compared to WT controls (Fig. 2C). Flow cytometry of TILs extracted from dissected whole tumor tissue revealed a significant increase in the frequency of CD11c^{+} cells in *Erk1*$^{-/-}$ mice (28.1 % in WT and 42.1 % in *Erk1*$^{-/-}$ mice, p=0.0473; Fig. 2D). More than 10 % of this CD11c^{+} population took up rhodamine-^{19}F particles *in vivo*, representing cells that had infiltrated tumor tissue from the periphery. Notably, the number of CD11c^{+}/^{19}F rhodamine^{+} leukocytes was significantly higher in *Erk1*$^{-/-}$ mice (2.7±0.4 % from whole TIL fraction in WT and 4.9±0.4 % in *Erk1*$^{-/-}$ mice, p=0.0057; Fig. 2D). Of note, a large proportion of CD11c^{+} cells was rhodamine negative (Fig. 2D), one reason being that CD11c is also expressed on brain resident cells such as microglia; these are abundantly present around the glioma tissue and could still be present after preparation of the tumor tissue for FACS analysis. Other than CD11c^{+}/^{19}F rhodamine^{+} cells, the CD3^{+}/CD8^{+} T cells from whole TIL fraction was also significantly higher in *Erk1*$^{-/-}$ mice compared to WT controls (3.1±0.6 % in WT and 10.7±2.2 % in *Erk1*$^{-/-}$ mice, p=0.0094; Fig. 2E), although the proportion of CD3^{+}/CD8^{+} T cells that took up ^{19}F rhodamine particles *in vivo* was very low (1-2 % of whole CD3^{+}/CD8^{+} population). This can be explained by the low phagocytic properties of T cells.

Overall, we demonstrate a significantly increased infiltration of CD11c^{+} immune cells and CD3^{+}/CD8^{+} T cells from the periphery into glioma tissue in *Erk1*$^{-/-}$ mice. The recruitment of CD11c^{+} immune cells and cytotoxic T cells into glioma tissue is necessary

11

for an efficient anti-tumor response (20, 21). Therefore, an increased proportion of immune cells in tumor tissue of *Erk1*^{-/-} mice (Fig. 2D and 2E) might explain the increased resilience of these mice towards developing gliomas (Fig. 1A) and their significantly increased rate of survival (Fig. 1B).

ERK1 deficiency enhances dendritic cell migration

The previous data (Fig. 2) show that a deficiency in ERK1 increases the accumulation of TILs. This is in line with previous findings that ERK activation after pharmacological inhibition of MEK-1 reduces DC migration towards the chemokines CCL21 (8), CCL19 and CXCL12 (22). However, MEK-1 phosphorylates both ERK1 and ERK2, and these isoforms — despite their striking homology — have explicitly different roles. Considering the role of ERKs, in general, in controlling cell migration (7), we next investigated the role of ERK1 in DC and T cell migration through *in vitro* migration assays. CXCL12 is highly expressed in brain tumors and is a potent chemoattractant of CXCR4-expressing immune cells, including DCs and T cells (23). A modified Boyden chamber assay revealed that in comparison to WT T cells, *Erk1*^{-/-} T cells exhibit a slight but not significant decrease in migration towards CXCL12 (Fig. 3A). MEK inhibition by UO126 (which inhibits both ERK1 and ERK2 activation) did not affect T cell migration in WT or *Erk1*^{-/-} T cells. In contrast, *Erk1*^{-/-} BMDC revealed significantly increased migration towards CXCL12 compared to WT BMDC (Fig. 3B). With the application of UO126, BMDC migrated to a slightly but not significantly lower extent towards CXCL12 (Fig. 3B). Migration inhibition following UO126 occurred at equal levels in WT and *Erk1*^{-/-} BMDC.

12

The chemokine CCL19 plays a key role in the trafficking of DCs into LNs (24). To confirm the role of ERK1 in DC migration, we applied another *in vitro* assay. We observed a significant increase in the numbers (>3 folds, ***$p<0.001$) of *Erk1*^{-/-} BMDC migrating towards CCL19-containing agarose spots 3 h after plating (Fig. 3C). Considering the increased migration of *Erk1*^{-/-} BMDC towards CCL19, we then studied expression of CCR7 on these cells to determine possible mechanisms for the increased migratory properties. However, we did not observe an increase in CCR7 expression in immature and mature *Erk1*^{-/-} BMDC when compared to WT BMDC (Fig. 3D).

Given that migration is an important feature for DC homing to lymphoid organs (24), we next developed a noninvasive *in vivo* DC migration assay involving $^{19}F/^{1}H$ MRI and a labeling of BMDC with ^{19}F nanoparticles *in vitro* prior to their application *in vivo* (25, 26). In a WT mouse, one limb received 5×10^{6} WT BMDC intradermally, and the other limb 5×10^{6} *Erk1*^{-/-} BMDC. Using this method we observed an increased migration of ^{19}F-labeled *Erk1*^{-/-} BMDC (compared to WT BMDC) towards WT popliteal LN as shown by the ^{19}F-signal in $^{19}F/^{1}H$ MRI (Fig. 4A). *Ex vivo* ^{19}F MR spectroscopy of the extracted popliteal LNs (Fig. 4A) revealed at least twice as many ^{19}F-labeled *Erk1*^{-/-} BMDC (26.1×10^{3} cells) reach the corresponding LNs compared to WT BMDC (11.8×10^{3} cells) ($p=0.028$; Fig. 4B).

We attributed the increase in the *in vivo* ^{19}F signal following *Erk1*^{-/-} BMDC application (Fig. 4A, 4B) and in *Erk1*^{-/-} gliomas (Fig. 2B, 2C) to an increase in cell mobilization in tissue. However an increased ^{19}F-signal could also be the result of an increased ^{19}F nanoparticle uptake by *Erk1*^{-/-} DC, inspite of our previous observations showing that *Erk1*^{-/-} BMDC are more mature than WT BMDC (11). We then measured phagocytosis in BMDC following overnight incubation with ^{19}F nanoparticles (same protocol as for the *in*

13

vivo experiments) by performing ^{19}F MR spectroscopy. We did not observe any significant differences between WT and *Erk1*$^{-/-}$ BMDC to take up ^{19}F nanoparticles (Fig. 4C). We also did not observe any influence of the ^{19}F nanoparticles themselves to significantly alter the phagocytic or migratory properties of both WT and *Erk1*$^{-/-}$ BMDC (data not shown).

ERK1 controls cytoskeletal changes in DCs

The Rho GTPase Cdc42 is a master regulator of DC polarity and is thus necessary for processes such as the reorientation of the microtubule-organizing center during endocytosis (27) and leading-edge coordination as decisive factors for DC motility *in vivo* (28). Interestingly, DCs have been shown to down-regulate Cdc42 activity following activation (27). To determine ERK1's effects on Cdc42 regulation during DC migration, we performed Cdc42 activity assays in *Erk1*$^{-/-}$ and WT BMDC. Surprisingly, while Cdc42 activity was down-regulated in WT BMDC, this was not the case for *Erk1*$^{-/-}$ BMDC following stimulation with CXCL12 chemokine (Fig. 5A).

Altogether our findings (Fig. 3, 5A, 5B) suggest that DC polarization is increased in the absence of ERK1. We thus measured filamentous actin (f-actin) in BMDC by FACS and found larger quantities of f-actin in *Erk1*$^{-/-}$ BMDC compared to WT BMDC (Fig. 5B).

The large cytoskeletal protein talin is an adaptor protein associated with actin filaments and is required for actin polymerization. Immunofluorescence microscopy revealed an increase in cytoskeletal protrusions and a denser expression of f-actin and talin in *Erk1*$^{-/-}$ BMDC, particularly within the intracellular compartment (Fig. 5C). This indicates a higher level of cytoskeleton organization in *Erk1*$^{-/-}$ BMDC and might explain our observations of an increase in their motility and migratory potential *in vitro* (Fig. 3) and

14

in vivo (Fig. 4). Furthermore, the actin-bundling protein fascin1 is selectively expressed on DCs upon maturation (29) and is critical for the assembly of filopodia, thereby increasing cell motility (30). As shown in Fig. 5D (upper row), immature BMDC expressed lower levels of fascin1 in WT and *Erk1*$^{-/-}$ BMDC. Upon LPS-induced maturation, fascin1 expression was upregulated, an effect that was more pronounced in *Erk1*$^{-/-}$ compared to WT BMDC (Fig. 5D, lower row).

Our data indicate that in contrast to WT BMDC, *Erk1*$^{-/-}$ BMDC maintain a high level of Cdc42 activity following activation and exhibit an abundantly polymerized cytoskeleton with fully assembled filopodia. This might aid the infiltration of DCs into tumor tissue (Fig. 2C and 2D). We also investigated the expression of fascin1 in CD11c$^+$ cells that infiltrated glioma tissue. In glioma-bearing *Erk1*$^{-/-}$ mice, the number of fascin1-expressing CD11c$^+$ DCs in TILs isolated from dissected glioma tissue (18 dpi) was significantly higher than that from glioma tissue from WT mice (Fig. 5E, p=0.00334). These data provide further evidence of increased DC migration in the absence of ERK1, which could indicate a more potent anti-tumor response in ERK1-deficient DCs.

ERK1 deficiency does not influence DC-T cell interaction

A successful immune response to tumors depends on an effective crosstalk between DCs and T cells in priming tumor-specific CD8$^+$ T cells (31). Since Cdc42-associated pathways are also necessary for microtubule-organizing center reorientation in DCs during antigen presentation to T cells (32), we investigated whether *Erk1*$^{-/-}$ BMDC mount a more potent anti-tumor T cell response. To explore this, we generated OVA-GL261 and transduced T cells with a T cell receptor (TCR) that specifically recognizes OVA-derived peptide in the context of MHC I (H-2Kb) (please refer to Supplementary Methods). To

test the specificity of the OVA-GL261 system, we stereotactically implanted OVA-GL261 cells into the striatum of WT mice and OT1 mice (CD8 T cell TCR-transgenic recognizing OVA). Fourteen days following tumor cell inoculation, MRI revealed OVA-GL261-induced glioma formation in the WT mice (Fig. 6A, left) but no sign of tumor formation in the OT1 mice (Fig. 6A, right). This confirmed the tumorigenicity of the OVA-GL261 glioma cells and efficient antigen recognition by OT1 T cells.

We next investigated the capacity of *Erk1*^{-/-} BMDC to cross-prime T cells. BMDC were isolated from WT and *Erk1*^{-/-} mice and then pulsed with various antigens (LPS, OVA peptide, or OVA-GL261 lysate). Following co-culture with OT1-transduced T cells, we measured the secretion of IFN-gamma (IFNg) by ELISA. Secretion of IFNg has been proven to reflect both the extent of DC-mediated T cell cross-priming as well as cytotoxic properties of tumor antigen-specific CD8^{+} T cells (33). We did not observe any differences between the capacity of WT and *Erk1*^{-/-} BMDC to prime IFNg secretion in tumor-specific T cells (Fig. 6B).

ERK1 deficiency enhances antitumor activity of DC vaccines against high-grade glioma

Brain tumor regression requires the recruitment of functional DCs into the glioma microenvironment (20). Since we observed a higher migratory potential of *Erk1*^{-/-} BMDC *in vivo*, we next asked whether ERK1 deficiency might have a beneficial impact on DC vaccination in GBM. To examine the therapeutic efficacy of *Erk1*^{-/-} BMDC, we vaccinated glioma-bearing mice twice a week with WT or *Erk1*^{-/-} BMDC, which were pulsed with GL261 lysate, and performed ^{1}H MRI 18 dpi (Fig. 7A). The size of tumors in glioma-bearing mice that received WT BMDC was slightly smaller than PBS treated

glioma-bearing mice (20 ± 5 mm^3 and 30.9 ± 2.8 mm^3, respectively; p=0.0803). On the other hand, tumor size in glioma-bearing mice that received *Erk1$^{-/-}$* BMDC vaccines (8.4 ± 2.9 mm^3; p=0.000035 when compared to PBS group) was significantly smaller than in untreated glioma-bearing mice (Fig. 7B, right panel). Notably, WT BMDC did not show a significant effect on tumor size reduction at this time point (18 dpi). Consistent with previous observations made in glioma-bearing mice (34), mice receiving WT BMDC pulsed with GL261 lysate still exhibited significantly enhanced survival when compared to untreated PBS controls (Fig. 7C). When compared with the untreated PBS group, WT BMDC had a higher survival probability (p=0.0019). Furthermore, in line with a markedly decreased tumor size, we documented significantly improved survival probability in glioma-bearing mice receiving *Erk1$^{-/-}$* BMDC compared to those of untreated mice (p=0.0005) (Fig. 7C).

We next wanted to study the distribution of both *Erk1$^{-/-}$* and WT BMDC in the glioma model following intraperitoneal application (Fig. 7D). For this we employed BMDC that were derived from either (*Erk1$^{-/-}$* $\times$ *tdRFP*) mice or (*Erk1$^{+/+}$*(WT)$\times$ *tdRFP*) littermate control mice. Although we could not detect any of the injected RFP BMDC (both WT and *Erk1$^{-/-}$*) in the brain of glioma mice 21 dpi, we observed a significant increase in CD11c$^+$ RFP$^+$ BMDC in the lymph nodes of mice treated with (*Erk1$^{-/-}$* $\times$ *tdRFP*) BMDC when compared to mice treated with (*Erk1$^{+/+}$*(WT)$\times$ *tdRFP*) BMDC (Fig. 7D). These results in the glioma model are in line with our *in vitro* assays (Fig. 3) and *in vivo* experiments in WT healthy mice (Fig. 4A).

Although we could not detect any of the intraperitoneally-administered (WT or *Erk1$^{-/-}$*) BMDC in the brain of glioma-bearing mice, we observed differences in the expression of tumor-infiltrating CD8$^+$ T cells between the different treatment groups (Fig. 7E). While

17

tumor sections demonstrated visibly smaller tumors when treated with BMDC, the number of CD8$^+$ T cells was significantly increased in sections derived from mice treated with WT BMDC compared to PBS-treated groups (1359±39 cells/mm^2 and 716±24 cells/mm^2, respectively; p=0.001). The infiltration of CD8$^+$ cells was further enhanced when treating mice with *Erk1$^{-/-}$* BMDC (1920±49 cells/mm^2; p=0.02 when compared to WT BMDC) (Fig. 7E).

Discussion

In this report, we identify ERK1 as a regulator of DC migration and show that the introduction of DCs lacking ERK1 lead to a significant reduction in tumor growth as well as improved survival of glioma-bearing mice.

DCs need to actively migrate between lymphatic tissue and interstitial spaces to initiate adaptive immune responses. Here we demonstrate that ERK1 plays a crucial role in the migratory capacity of DCs. This key ERK-MAPK intracellular signaling pathway transduces a broad range of extracellular stimuli into important biological responses including cell survival, proliferation, differentiation, and the regulation of DCs (9, 35) and T cells (36). The specific role of ERK1 has been studied in T cells and it was shown that ERK1 does not appear to play a direct role on the effector function of antigen-specific T cells, notwithstanding increased susceptibility towards T cell mediated autoimmunity (37). In DCs, ERK1 inhibits cytokine production following their stimulation by TLRs (38) and reduces surface receptors (11), which in turn affects the priming of naïve T cells towards an effector phenotype during autoimmunity (11). Most studies of tumor pathology have not distinguished ERK1 from ERK2 function, due to the assumption that they have compensatory effects (39). However, in some biological contexts the distinction between these two kinases appears to be crucial, considering that ERK2-deficient mice are embryonically lethal (40) in contrast to ERK1-deficient mice, which are viable and fertile (12). Here we report for the first time a role for ERK1 in negatively regulating the migration specifically of DCs by showing a significant increase in migration in *Erk1$^{-/-}$* BMDC, both in *in vitro* and *in vivo* experiments. *In vitro*, we distinguished between the impact of ERK1 on BMDC and effector T cells. Although ERK1 is expressed in both cell types, its role in migration was more pronounced in DC

19

than in T cells. Furthermore, while ERK1 deletion promoted DC migration, application of a MEK inhibitor (U0126) inhibited DC migration. Since U0126 inhibits both ERK1 and ERK2 activation, this might have masked the increase in migration we observe in the absence of ERK1 and could furthermore explain discrepancies in earlier studies using inhibitors to ascertain the signals' roles in migration-related processes (41).

Migratory phenotypes typically involve mechanisms related to cytoskeletal organization and structure, so we studied this aspect of ERK1's influence. We showed that ERK1 influences the cytoskeleton and associated adaptor and actin-bundling proteins such as talin and fascin1, another strong piece of evidence for a role of ERK1 in the regulation of DC migration. We chose fascin1 as a marker for dendritic cells in the tumor tissue, since CD11c$^+$ is not an exclusive marker for these cells in brain gliomas: CNS resident and non-resident immune cells such as peripheral macrophages (42) are also CD11c$^+$. Importantly, fascin1 is not expressed on activated microglia (43) and peripheral blood cells, including macrophages and neutrophils (44).

A role for ERK1 in DC migration is additionally supported by our finding that ERK1 deletion promotes Cdc42 activation, since Cdc42 is responsible for leading edge coordination *in vivo* (28). Notwithstanding the role of Cdc42 in DC polarity and orientation during antigen presentation to T cells (32), *Erk1$^{-/-}$* DCs did not present OVA-GL261 (as model-tumor antigen) to T cells more effectively than WT DCs. This excludes tumor antigen presentation as an underlying mechanism for the decreased susceptibility of *Erk1$^{-/-}$* mice to develop gliomas and for the increased infiltration of T cells in WT gliomas in these mice compared to WT mice. The observation indicates that the benefits of ERK1 deficiency in reducing the growth of gliomas likely derive from an ultimate increase in immune cell surveillance in the glioma tissue as shown by an increase in

20

CD11c$^+$ leukocytes, fascin1$^+$ DCs and CD8$^+$ T cells in *Erk1$^{-/-}$* glioma-bearing mice as well as increase in CD8$^+$ T cells in *Erk1$^{-/-}$* BMDC-treated glioma-bearing mice. From our results, we believe that ERK1 deficiency is better adapted for providing a higher availability/localization of BMDC in the periphery rather than increasing tumor antigen presentation and therefore priming of antigen-specific cytotoxic T cells. Although we did not detect the administered *Erk1$^{-/-}$* BMDC in the tumor tissue following therapeutic application in the glioma model, we did observe a significantly increased proportion of *Erk1$^{-/-}$* RFP$^+$ cells in the LNs and an increased CD8$^+$ population of T cells infiltrating the tumor tissue.

Ultimately, improved immune cell surveillance would also augment the reactivation and expansion of cytotoxic T cells within tumor-relevant sites. Our results suggest that the enhanced therapeutic properties of *Erk1$^{-/-}$* BMDC could be the result of an improvement in the delivery of *Erk1$^{-/-}$* BMDC to the lymphatic tissue which eventually results in a larger infiltration of CD8$^+$ T cells into the tumor tissue. A recent NIH-funded clinical trial found that improving the LN homing of DCs in GBM patients significantly enhances the therapeutic efficacy of tumor antigen–loaded DCs (45). Their finding and our study suggest that monitoring DC migration might deliver a predictive readout for the effectiveness of DC vaccines.

Here we used ^{19}F MR to do this, and although still in early clinical development (46), it might offer significant advantages in the future over other methods to track DC migration such as scintigraphy combined with radioisotope ^{111}In-oxine (47). MRI in general was shown to be better at localizing DC vaccines *in vivo* (48); paramagnetic iron oxide nanoparticles were used to label and follow cells in melanoma patients (48). Even though this represented a major step forward in the tracking of DCs, lower image contrast often

makes it difficult to distinguish MRI signal hypointensities originating from magnetically-labeled cells from hypointensities caused by endogenous factors (e.g. deoxygenated blood). ^{19}F MR-based methods were simultaneously introduced in animal models to overcome these hurdles in cellular MR imaging (49).

The elegance of ^{19}F MR lies in the fact that it provides background-free images in mammals and permits a highly selective detection of cells *in vivo* throughout the organism's body (50). The main hurdle is signal sensitivity, which can pose a challenge when imaging ^{19}F-labeled DCs in cancer patients (46). In a recent report we aimed to promote the signal achieved per unit cell; we enriched ^{19}F nanoparticles with the phosphatidylethanolamine DPPE and observed a stronger enhancement of ^{19}F signal (from 74 nmol to 771 nmol) per 10^6 cells, which equates to an order of magnitude increase in ^{19}F spins from 0.89×10^{12} ^{19}F spins (control nanoparticles) to 0.93×10^{13} ^{19}F spins (in DPPE-enriched nanoparticles) per DC unit (19). In the present study we made use of the recently developed ^{19}F marker (19) to label and track DCs *in vivo* with greater sensitivity and to determine the role of ERK1 in DC migration.

We can follow the ^{19}F signal from DCs that we had administered and showed that *Erk1$^{-/-}$* DCs migrate more readily than WT DCs into popliteal LNs. We also quantified the ^{19}F signal and thereby the number of DCs in draining LNs by *ex vivo* ^{19}F MRS and observed a significant increase in the number of *Erk1$^{-/-}$* DCs compared to WT DCs that appeared in the corresponding draining LNs. While further developments in ^{19}F MR will be needed to expand its use in clinical applications (51), it is a valuable tool to monitor DC homing in cancer therapy and to effectively interpret the *in vivo* distribution of DCs as a means of assessing the effectiveness of these therapies in GBM patients. The advent of cryogenically cooled MR detectors (52) will help boost ^{19}F MR sensitivity and lower

22

detection levels of ^{19}F-labeled cells to facilitate *in vivo* cell tracking within shorter scan times.

Here we identified ERK1 as a molecular player that negatively regulates the mobility of DCs and their capacity to eliminate malignant gliomas. The results were demonstrated in a preclinical mouse GBM model and further studies will be required to predict the safety, efficacy and potential benefits of *Erk1$^{-/-}$* DC vaccines in human high-grade or recurrent gliomas. While the present study is restricted to the role of ERK1 against GBM, effective therapies will likely need to target the tumor from many different angles, employing several approaches toward tumor cell elimination while preserving sufficient natural anti-tumor immune responses. Other strategies such as the preconditioning of application sites with recall antigen to promote DC vaccination in humans and mice (45), as recently reported further emphasizes the need to promote DC migration as a means of optimizing DC vaccines. As negative regulator of DC migration, ERK1 appears to be an attractive target for deletion in genetically modified vaccines. Other possible molecular targets include molecules such as IRF4 (53) and CD37 (54), which favor DC migration. It has now become practical to apply simultaneous gene silencing and retroviral transgenic insertion; such combinations have proven to be highly effective (55, 56). *Ex vivo* gene silencing in immune cell therapeutics using both viral and non-viral based approaches has been an area of intensive research in clinical trials during the last decade (57)

In summary, our study demonstrates the advantage of specific gene manipulation in DC vaccines to promote their migration and efficacy in reducing tumor progression in an animal model of GBM. Furthermore, this study underscores the benefits and needs of using ^{19}F MRI to measure *in vivo* cell migration and localization, which are critical parameters in the effectiveness of such vaccines. ERK1 and other molecular targets that

23

enhance DC migration will be important tools in developing a next generation of DC vaccines (45). The overall survival of GBM patients could well be improved by patient-specific treatment regimens that use immunotherapy based on genetically modified cells in conjunction with standard treatment protocols (surgery, radiotherapy, chemotherapy, and anti-angiogenic therapy).

Acknowledgement

We thank S. Kox and Y. Balke for assistance with MR measurements and cell culturing, and M. Naschke for assistance with ELISA measurements. We also thank the support of the Animal Facilities and the technology platforms for Advanced Light Microscopy and Preparative Flow Cytometry of the Max Delbrück Center for Molecular Medicine. We are also grateful to Prof. K. Rajewsky for valuable discussions and scientific writer R. Hodge for support in manuscript editing.

References

1. Weller M, Cloughesy T, Perry JR, Wick W. Standards of care for treatment of recurrent glioblastoma—are we there yet? Neuro-Oncology. 2013;15:4-27.

2. Hardee ME, Zagzag D. Mechanisms of Glioma-Associated Neovascularization. The American journal of pathology. 2012;181:1126-41.

3. Rabinovich GA, Gabrilovich D, Sotomayor EM. IMMUNOSUPPRESSIVE STRATEGIES THAT ARE MEDIATED BY TUMOR CELLS. Annual review of immunology. 2007;25:267-96.

4. Anguille S, Smits EL, Lion E, van Tendeloo VF, Berneman ZN. Clinical use of dendritic cells for cancer therapy. The Lancet Oncology. 2014;15:e257-67.

5. Palucka AK, Ueno H, Fay JW, Banchereau J. Taming cancer by inducing immunity via dendritic cells. Immunol Rev. 2007;220:129-50.

6. Aarntzen EH, Srinivas M, Bonetto F, Cruz LJ, Verdijk P, Schreibelt G, et al. Targeting of 111In-labeled dendritic cell human vaccines improved by reducing number of cells. Clinical cancer research : an official journal of the American Association for Cancer Research. 2013;19:1525-33.

7. Webb DJ, Donais K, Whitmore LA, Thomas SM, Turner CE, Parsons JT, et al. FAK-Src signalling through paxillin, ERK and MLCK regulates adhesion disassembly. NatCell Biol. 2004;6:154-61.

8. Luft T, Maraskovsky E, Schnurr M, Knebel K, Kirsch M, Gorner M, et al. Tuning the volume of the immune response: strength and persistence of stimulation determine migration and cytokine secretion of dendritic cells. Blood. 2004;104:1066-74.

9. Arce F, Breckpot K, Stephenson H, Karwacz K, Ehrenstein MR, Collins M, et al. Selective ERK activation differentiates mouse and human tolerogenic dendritic cells,

expands antigen-specific regulatory T cells, and suppresses experimental inflammatory arthritis. Arthritis & Rheumatism. 2011;63:84-95.

10. Fischer AM, Katayama CD, Pages G, Pouyssegur J, Hedrick SM. The role of erk1 and erk2 in multiple stages of T cell development. Immunity. 2005;23:431-43.

11. Bendix I, Pfueller CF, Leuenberger T, Glezeva N, Siffrin V, Muller Y, et al. MAPK3 deficiency drives autoimmunity via DC arming. European journal of immunology. 2010;40:1486-95.

12. Pages G, Guerin S, Grall D, Bonino F, Smith A, Anjuere F, et al. Defective thymocyte maturation in p44 MAP kinase (Erk 1) knockout mice. Science. 1999;286:1374-7.

13. Luche H, Weber O, Nageswara Rao T, Blum C, Fehling HJ. Faithful activation of an extra-bright red fluorescent protein in "knock-in" Cre-reporter mice ideally suited for lineage tracing studies. European journal of immunology. 2007;37:43-53.

14. Ku MC, Wolf SA, Respondek D, Matyash V, Pohlmann A, Waiczies S, et al. GDNF mediates glioblastoma-induced microglia attraction but not astrogliosis. Acta neuropathologica. 2013;125:609-20.

15. Waiczies S, Bendix I, Prozorovski T, Ratner M, Nazarenko I, Pfueller CF, et al. Geranylgeranylation but not GTP loading determines rho migratory function in T cells. JImmunol. 2007;179:6024-32.

16. Waiczies H, Lepore S, Drechsler S, Qadri F, Purfurst B, Sydow K, et al. Visualizing brain inflammation with a shingled-leg radio-frequency head probe for 19F/1H MRI. Scientific reports. 2013;3:1280.

17. Charles NA, Holland EC, Gilbertson R, Glass R, Kettenmann H. The brain tumor microenvironment. Glia. 2011;59:1169-80.

27

18. Flögel U, Ding Z, Hardung H, Jander S, Reichmann G, Jacoby C, et al. In vivo monitoring of inflammation after cardiac and cerebral ischemia by fluorine magnetic resonance imaging. Circulation. 2008;118:140-8.

19. Waiczies S, Lepore S, Sydow K, Drechsler S, Ku MC, Martin C, et al. Anchoring dipalmitoyl phosphoethanolamine to nanoparticles boosts cellular uptake and fluorine-19 magnetic resonance signal. Scientific reports. 2015;5:8427.

20. Curtin JF, Liu N, Candolfi M, Xiong W, Assi H, Yagiz K, et al. HMGB1 Mediates Endogenous TLR2 Activation and Brain Tumor Regression. PLoS Med. 2009;6:e1000010.

21. Candolfi M, King GD, Yagiz K, Curtin JF, Mineharu Y, Muhammad AK, et al. Plasmacytoid dendritic cells in the tumor microenvironment: immune targets for glioma therapeutics. Neoplasia. 2012;14:757-70.

22. Li G, Basu S, Han MK, Kim YJ, Broxmeyer HE. Influence of ERK activation on decreased chemotaxis of mature human cord blood monocyte-derived dendritic cells to CCL19 and CXCL12. Blood. 2007;109:3173-6.

23. Li M, Ransohoff RM. Multiple roles of chemokine CXCL12 in the central nervous system: A migration from immunology to neurobiology. Progress in Neurobiology. 2008;84:116-31.

24. Randolph GJ, Angeli V, Swartz MA. Dendritic-cell trafficking to lymph nodes through lymphatic vessels. Nature reviews Immunology. 2005;5:617-28.

25. Ahrens ET, Flores R, Xu H, Morel PA. In vivo imaging platform for tracking immunotherapeutic cells. NatBiotechnol. 2005;23:983-7.

26.   Waiczies H, Lepore S, Janitzek N, Hagen U, Seifert F, Ittermann B, et al. Perfluorocarbon particle size influences magnetic resonance signal and immunological properties of dendritic cells. PloS one. 2011;6:e21981.

27.   Garrett WS, Chen LM, Kroschewski R, Ebersold M, Turley S, Trombetta S, et al. Developmental control of endocytosis in dendritic cells by Cdc42. Cell. 2000;102:325-34.

28.   Lammermann T, Renkawitz J, Wu X, Hirsch K, Brakebusch C, Sixt M. Cdc42-dependent leading edge coordination is essential for interstitial dendritic cell migration. Blood. 2009;113:5703-10.

29.   Yamashiro S. Functions of fascin in dendritic cells. Critical reviews in immunology. 2012;32:11-21.

30.   Yamakita Y, Matsumura F, Lipscomb MW, Chou PC, Werlen G, Burkhardt JK, et al. Fascin1 promotes cell migration of mature dendritic cells. Journal of immunology. 2011;186:2850-9.

31.   Gajewski TF, Schreiber H, Fu Y-X. Innate and adaptive immune cells in the tumor microenvironment. Nature immunology. 2013;14:1014-22.

32.   Pulecio J, Petrovic J, Prete F, Chiaruttini G, Lennon-Dumenil A-M, Desdouets C, et al. Cdc42-mediated MTOC polarization in dendritic cells controls targeted delivery of cytokines at the immune synapse. The Journal of experimental medicine. 2010;207:2719-32.

33.   Wheeler CJ, Black KL, Liu G, Mazer M, Zhang XX, Pepkowitz S, et al. Vaccination elicits correlated immune and clinical responses in glioblastoma multiforme patients. Cancer research. 2008;68:5955-64.

34.   Ni HT, Spellman SR, Jean WC, Hall WA, Low WC. Immunization with dendritic cells pulsed with tumor extract increases survival of mice bearing intracranial gliomas. Journal of neuro-oncology. 2001;51:1-9.

35.   Escors D, Lopes L, Lin R, Hiscott J, Akira S, Davis RJ, et al. Targeting dendritic cell signaling to regulate the response to immunization. Blood. 2008;111:3050-61.

36.   Waiczies S, Prozorovski T, Infante-Duarte C, Hahner A, Aktas O, Ullrich O, et al. Atorvastatin Induces T Cell Anergy via Phosphorylation of ERK1. JImmunol. 2005;174:5630-5.

37.   Nekrasova T, Shive C, Gao Y, Kawamura K, Guardia R, Landreth G, et al. ERK1-deficient mice show normal T cell effector function and are highly susceptible to experimental autoimmune encephalomyelitis. J Immunol. 2005;175:2374-80.

38.   Agrawal A, Dillon S, Denning TL, Pulendran B. ERK1-/- mice exhibit Th1 cell polarization and increased susceptibility to experimental autoimmune encephalomyelitis. J Immunol. 2006;176:5788-96.

39.   Blasco RB, Francoz S, Santamaria D, Canamero M, Dubus P, Charron J, et al. c-Raf, but not B-Raf, is essential for development of K-Ras oncogene-driven non-small cell lung carcinoma. Cancer Cell. 2011;19:652-63.

40.   Hatano N, Mori Y, Oh-hora M, Kosugi A, Fujikawa T, Nakai N, et al. Essential role for ERK2 mitogen-activated protein kinase in placental development. Genes Cells. 2003;8:847-56.

41.   Fincham VJ, James M, Frame MC, Winder SJ. Active ERK/MAP kinase is targeted to newly forming cell-matrix adhesions by integrin engagement and v-Src. EMBO J. 2000;19:2911-23.

42.   Parney IF, Waldron JS, Parsa AT. Flow cytometry and in vitro analysis of human glioma–associated macrophages. Journal of neurosurgery. 2009;110:572-82.

43.   Gao Z, Tsirka SE. Animal Models of MS Reveal Multiple Roles of Microglia in Disease Pathogenesis. Neurol Res Int. 2011;2011:383087.

44.   Mosialos G, Birkenbach M, Ayehunie S, Matsumura F, Pinkus GS, Kieff E, et al. Circulating human dendritic cells differentially express high levels of a 55-kd actin-bundling protein. Am J Pathol. 1996;148:593-600.

45.   Mitchell DA, Batich KA, Gunn MD, Huang MN, Sanchez-Perez L, Nair SK, et al. Tetanus toxoid and CCL3 improve dendritic cell vaccines in mice and glioblastoma patients. Nature. 2015;519:366-9.

46.   Ahrens ET, Helfer BM, O'Hanlon CF, Schirda C. Clinical cell therapy imaging using a perfluorocarbon tracer and fluorine-19 MRI. Magnetic Resonance in Medicine. 2014.

47.   De Vries IJ, Krooshoop DJ, Scharenborg NM, Lesterhuis WJ, Diepstra JH, Van Muijen GN, et al. Effective migration of antigen-pulsed dendritic cells to lymph nodes in melanoma patients is determined by their maturation state. Cancer research. 2003;63:12-7.

48.   de Vries IJ, Lesterhuis WJ, Barentsz JO, Verdijk P, van Krieken JH, Boerman OC, et al. Magnetic resonance tracking of dendritic cells in melanoma patients for monitoring of cellular therapy. Nature biotechnology. 2005;23:1407-13.

49.   Ahrens ET, Flores R, Xu H, Morel PA. In vivo imaging platform for tracking immunotherapeutic cells. Nature biotechnology. 2005;23:983-7.

50.   Ahrens ET, Bulte JW. Tracking immune cells in vivo using magnetic resonance imaging. Nature reviews Immunology. 2013;13:755-63.

51.   Ji Y, Waiczies H, Winter L, Neumanova P, Hofmann D, Rieger J, et al. Eight-channel transceiver RF coil array tailored for 1H/19F MR of the human knee and fluorinated drugs at 7.0 T. NMR in Biomedicine. 2015.

52.   Niendorf T, Pohlmann A, Reimann HM, Waiczies H, Peper E, Huelnhagen T, et al. Advancing Cardiovascular, Neurovascular and Renal Magnetic Resonance Imaging in Small Rodents Using Cryogenic Radiofrequency Coil Technology. Frontiers in Pharmacology. 2015;6.

53.   Bajaña S, Roach K, Turner S, Paul J, Kovats S. IRF4 Promotes Cutaneous Dendritic Cell Migration to Lymph Nodes during Homeostasis and Inflammation. The Journal of Immunology. 2012;189:3368-77.

54.   Gartlan KH, Wee JL, Demaria MC, Nastovska R, Chang TM, Jones EL, et al. Tetraspanin CD37 contributes to the initiation of cellular immunity by promoting dendritic cell migration. European journal of immunology. 2013;43:1208-19.

55.   Bunse M, Bendle GM, Linnemann C, Bies L, Schulz S, Schumacher TN, et al. RNAi-mediated TCR Knockdown Prevents Autoimmunity in Mice Caused by Mixed TCR Dimers Following TCR Gene Transfer. Mol Ther. 2014;22:1983-91.

56.   Cox DBT, Platt RJ, Zhang F. Therapeutic genome editing: prospects and challenges. Nature medicine. 2015;21:121-31.

57.   Burnett John C, Rossi John J. RNA-Based Therapeutics: Current Progress and Future Prospects. Chemistry & Biology. 2012;19:60-71.

Figure legends

Figure 1 *Erk1^{-/-}* mice have a restricted glioma growth. (A) *Left panel*: MRI images of glioma bearing WT and *Erk1^{-/-}* mice were acquired 14 days following intracranial implantation of 2×10^4 GL261 cells using a 9.4 T animal MR system. Glioma tissue was segmented: white dashed line surrounds tumor area. *Right panel*: Following segmentation, a volumetric assessment of the glioma tissue was made in WT (n=11) versus *Erk1^{-/-}* mice brains (n=11). Error bars represent mean ± SEM; **, $p<0.01$. (B) Kaplan-Meier survival rate curves for both WT (n=11) and *Erk1^{-/-}* (n=11) glioma-bearing mice. Statistical significance was determined by log-rank testing, ***, $p<0.001$.

Figure 2 *Erk1^{-/-}* mice harbor more glioma-infiltrated leukocytes. (A) 18 dpi, rhodamine-^{19}F nanoparticles were injected into WT and *Erk1^{-/-}* glioma-bearing mice via tail vein 18 h prior to ^{19}F/^{1}H MRI. After ^{19}F/^{1}H MRI, WT and *Erk1^{-/-}* glioma-bearing mice were perfused to remove excess rhodamine-^{19}F nanoparticles and processed for *ex vivo* FACS or histology analysis. (B) *Left panel*: Representative ^{19}F/^{1}H MRI of glioma-bearing WT and *Erk1^{-/-}* mouse brains. Mouse brain anatomy (^{1}H grayscale image) is shown overlaid with immune cells labeled with rhodamine-^{19}F nanoparticles *in vivo* (^{19}F red pseudocolor image). Yellow dashed-line surrounds tumor area. *Right panel*: Intensity of ^{19}F signal from WT (n=8) and *Erk1^{-/-}* (n=8) glioma-bearing mice was normalized to tumor volume (^{19}F intensity/mm^3). Error bars represent mean ± SEM; **, $p<0.01$. (C) Representative immunofluorescent staining of CD11c (green) and rhodamine (red) signal in brain tumor sections of WT or *Erk1^{-/-}* mice, which were injected with rhodamine-^{19}F nanoparticles. Bars: 50 μm. (D) 18 dpi, TILs were isolated from WT and *Erk1^{-/-}* glioma-

bearing mice and analyzed by FACS. Representative dot plots of glioma-infiltrating CD11c$^+$ DCs and CD11c$^+$ DCs which also took up rhodamine-^{19}F nanoparticles. Percentage represents the cells from gating of living cells. (E) Representative dot plots of CD3$^+$/CD8$^+$ T cells from infiltrating TILs. All FACS data are representative of 5 independent experiments with pooled 3 mice per group. Values represent mean ± SEM; **, p<0.01.

Figure 3 ERK1 deficiency leads to increased DC migration *in vitro*. (A) WT or *Erk1$^{-/-}$* T cell migration towards CXCL12 was tested using a modified Boyden chamber. (B) WT or *Erk1$^{-/-}$* BMDC migration was also measured using the same method. Bars represent mean ± SEM; *, p<0.05; **, p<0.01. (C) Histogram overlay of CCR7 expression in WT or *Erk1$^{-/-}$* BMDC as measured by flow cytometry prior to and after maturation with LPS. (D) Representative light microscopic images of WT or *Erk1$^{-/-}$* BMDC (1×10^6 per plate) migrating towards CCL19. White dashed-lines represent the edge of agarose spot. White arrows depict the migration direction. *Right panel* shows quantified data from at least 3 independent experiments and at least 2 agarose spots per group. Error bars represent mean ± SEM; ***, p<0.001.

Figure 4 ERK1 deficiency leads to increased DC migration *in vivo*. (A) WT and *Erk1$^{-/-}$* BMDC labeled with ^{19}F nanoparticles were injected in the left (WT BMDC) and right (*Erk1$^{-/-}$* BMDC) footpad of WT mouse (n=13) and their migration towards the popliteal LNs imaged by ^{19}F/^{1}H MRI after 4 h. Mouse lower limb anatomy (^{1}H grayscale image) is shown overlaid with BMDC labeled with ^{19}F nanoparticles (^{19}F red pseudocolor image). (B) After ^{19}F/^{1}H MRI, both popliteal LNs were harvested and the number of ^{19}F-

labeled BMDC quantified by ^{19}F MR spectroscopy (MRS) of LNs and BMDC calibration samples. ^{19}F MR spectroscopy demonstrated significantly more ^{19}F-labeled DCs migrating in LNs for *Erk1$^{-/-}$* BMDC versus WT BMDC. Error bars represent mean ± SEM; *, $p<0.05$. (C) The phagocytic properties of WT and *Erk1$^{-/-}$* BMDC towards ^{19}F nanoparticles were compared by measuring the ^{19}F signal using ^{19}F MR spectroscopy for both groups in a calibration curve ranging from 5×10^4 to 5×10^6 BMDC.

Figure 5 *Erk1$^{-/-}$* BMDC display a more polarized cytoskeleton. (A) Activity of Cdc42 GTPase of WT and *Erk1$^{-/-}$* BMDC that were untreated or pretreated with CXCL12 was determined by pull-down assay and consecutive Western blot analysis (n=4). (B) Expression of intracellular f-actin on WT (solid line) or *Erk1$^{-/-}$* (filled black histogram) BMDC as assessed by FACS. Dashed line histograms depict control staining with anti-mouse IgG. Data represent 4 independent experiments. (C) Immunofluorescence staining of talin (green, left column), f-actin (red, middle) and Hoechst 33342 nuclei (blue, right) on WT and *Erk1$^{-/-}$* BMDC attached to glass coverslips. Bar, 10 μm. (D) Immunofluorescence staining of fascin1 (red) on WT and *Erk1$^{-/-}$* BMDC without (upper row) and with LPS stimulation (lower row). Data represent 3 independent experiments. Bar, 25 μm. (E) Representative dot plots of glioma-infiltrating fascin1-expressing CD11c$^+$ DC as determined by FACS. TILs were isolated from WT and *Erk1$^{-/-}$* glioma-bearing mice on 18 dpi. Data represent 5 independent experiments. Values represent mean ± SEM; **, $p<0.01$.

Figure 6 Antigen-specific T cell activation in *Erk1$^{-/-}$* BMDC remains unaltered. (A) MRI images show OVA-specificity: OVA-GL261 cells were inoculated in WT (n=3) or

OT1 transgenic mice (n=6) and tumor growth was monitored by ^{1}H MRI on 14 dpi. Yellow dashed-line surrounds tumor area in WT mouse. WT-GL261 transplanted in both WT mice (n=3) and OT1 transgenic mice (n=3) served as control (right panel). (B) WT and *Erk1*$^{-/-}$ BMDC were treated with OVA$_{SIINFEKL}$ peptide or OVA-GL261 cell lysate and then co-cultured with OT1-transduced T cells. OT1-T cells and non-transduced (WT) T cells were also cultured with PMA plus Ionomycin as positive control for IFNg production (right panel). Serving as negative controls (but are not shown) were non-transduced WT T cells activated by WT and *Erk1*$^{-/-}$ BMDC loaded with OVA$_{SIINFEKL}$ peptide or OVA-GL261 cell lysate, as well as untreated BMDC and LPS-treated BMDC. IFNg production was measured by ELISA. Data are representative of 3 independent experiments. Bars represent mean ± SEM.

Figure 7 *Erk1*$^{-/-}$ BMDC improve immunotherapy against high-grade glioma. (A) Schematic representation of DC vaccination protocol in glioma-bearing mice. (B) WT and *Erk1*$^{-/-}$ BMDC (2×10^6) loaded with 50 μg GL261 cell lysate and activated with LPS were administered to glioma-bearing WT mice via i.p. injection 3, 7, 10, and 14 dpi. Mice receiving PBS i.p. injections served as negative control. Tumor growth was validated 18 dpi by MRI. Data are representative of 3 independent experiments with at least 3 animals per group. Bars represent mean ± SEM; ***, p<0.001. (C) Kaplan-Meier survival curves were plotted for PBS (n=10), WT BMDC (n=10) and *Erk1*$^{-/-}$ BMDC (n=9) treated glioma animal groups. Statistical significance was determined by log-rank testing (**, p<0.01, WT BMDC vs PBS; ***, p<0.001, *Erk1*$^{-/-}$ BMDC vs PBS). (D) At 21 dpi, lymphocytes were isolated from glioma-bearing mice and analyzed for RFP$^+$ cells by FACS. All FACS data are from 2 independent experiments with 3 mice per group. Values

represent mean ± SEM; *, p<0.05. (E) Representative immunofluorescent staining of CD8a (red) and DAPI (blue) signal in brain tumor sections of WT mice, which were receiving either PBS, WT BMDC or *Erk1*^{-/-} BMDC. Bar: 50 μm. Yellow dashed-lines represent the edge of tumor. *Right panel* shows quantified cell number from 2 independent experiments with 2 animals per group. Bars represent mean ± SD; *, p<0.05, **, p<0.01.
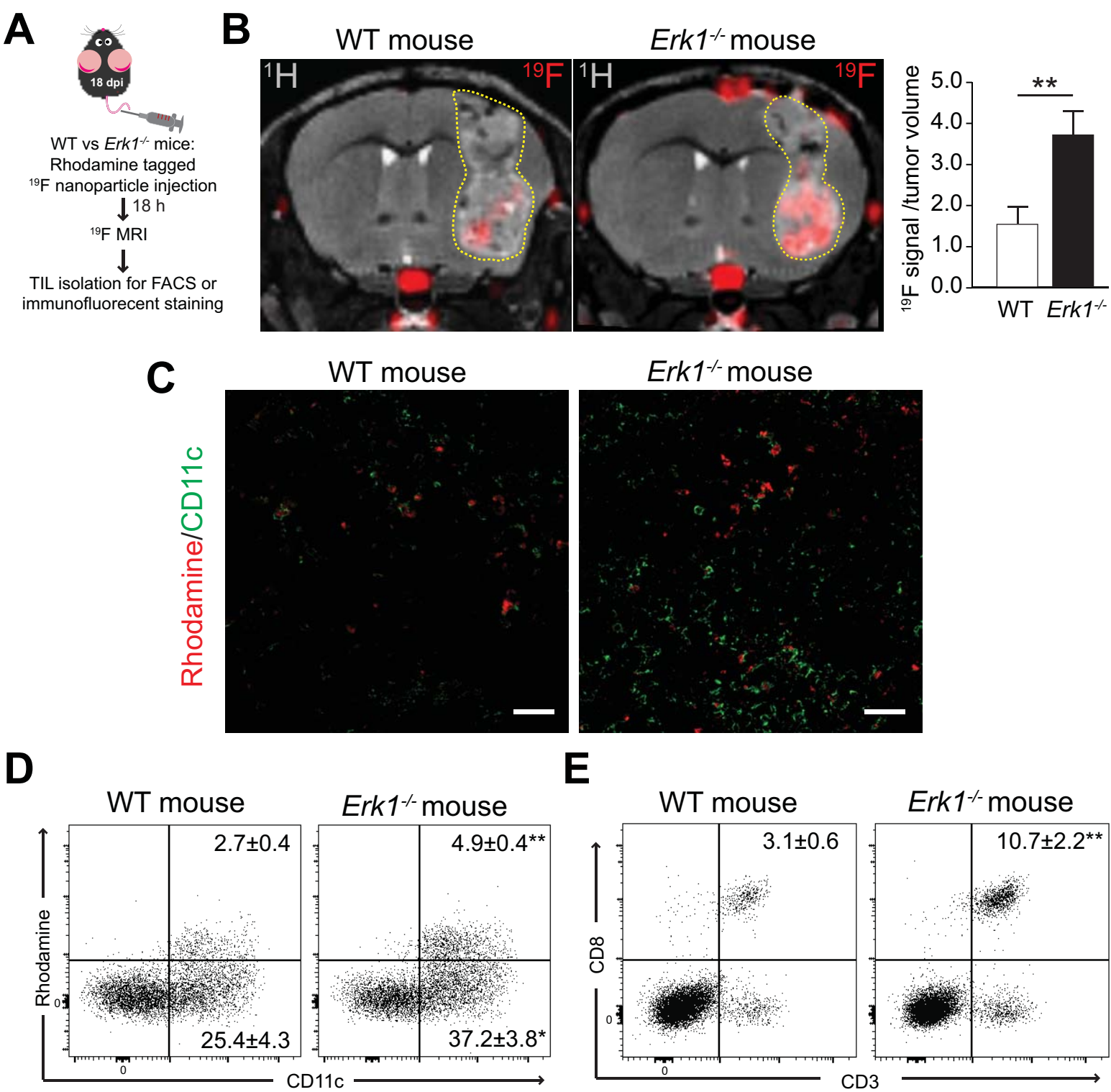
Figure 1

A

B

Figure 2

A 18 dpi

WT vs *Erk1*⁻/⁻ mice:
Rhodamine tagged
¹⁹F nanoparticle injection
↓ 18 h
¹⁹F MRI
↓
TIL isolation for FACS or
immunofluorecent staining

B

WT mouse   *Erk1*⁻/⁻ mouse

¹H   ¹⁹F   ¹H   ¹⁹F

C

WT mouse   *Erk1*⁻/⁻ mouse

Rhodamine/CD11c

D

WT mouse   *Erk1*⁻/⁻ mouse

Rhodamine

2.7±0.4   4.9±0.4**

25.4±4.3   37.2±3.8*

CD11c

E

WT mouse   *Erk1*⁻/⁻ mouse

CD8

3.1±0.6   10.7±2.2**

CD3

Figure 3

Figure 4

A

¹H/¹⁹F

WT BMDC   *Erk1^{-/-}* BMDC

B

*

WT   *Erk1^{-/-}*

¹⁹F-labeled DC migrating in LNs (X1000)

C

□ WT T cell
■ *Erk1^{-/-}* T cell

PFCE amount per sample (nmol)

Number of ¹⁹F-labeled BMDC (x1000)
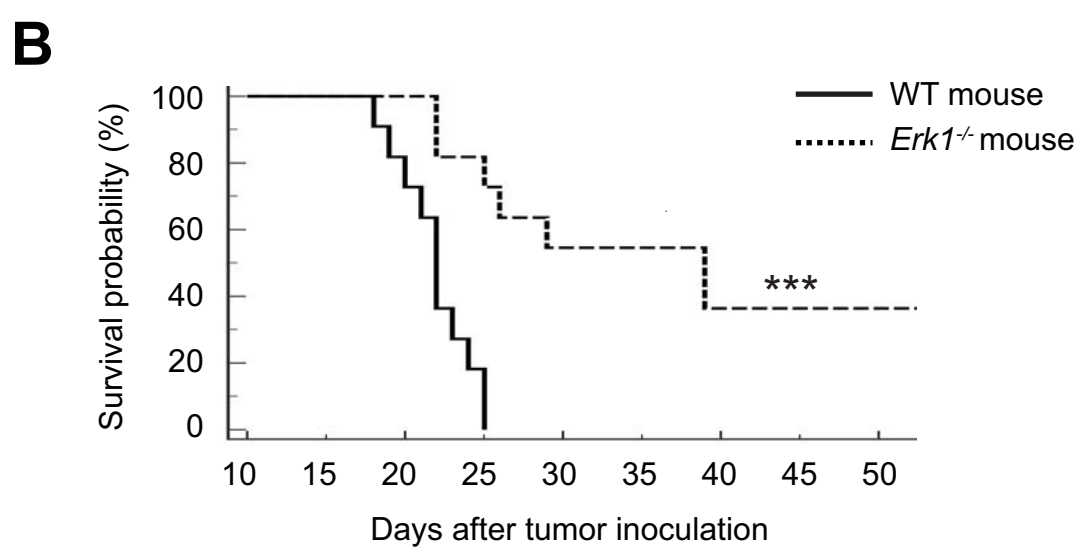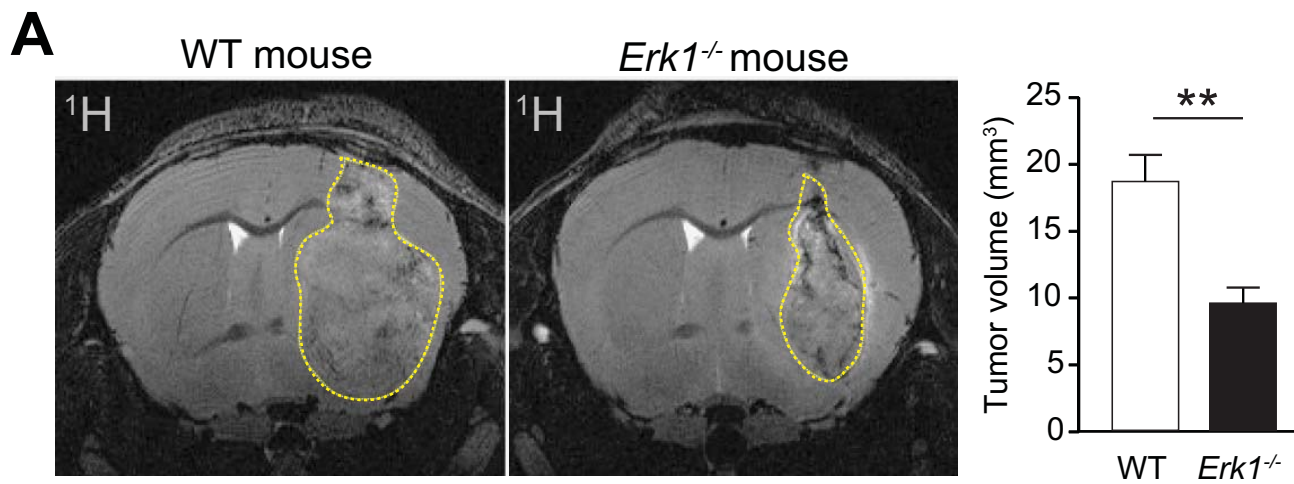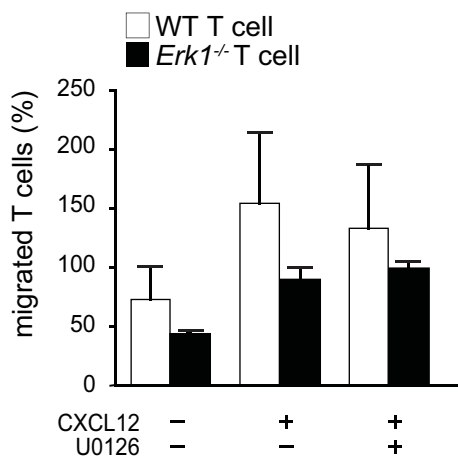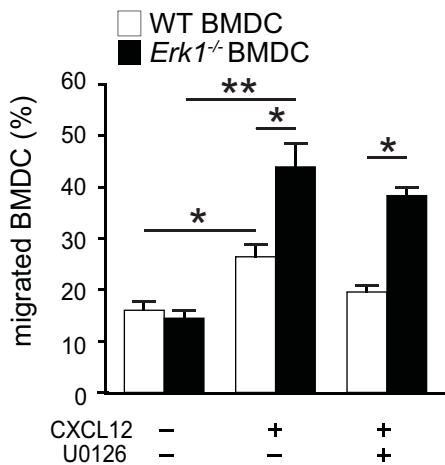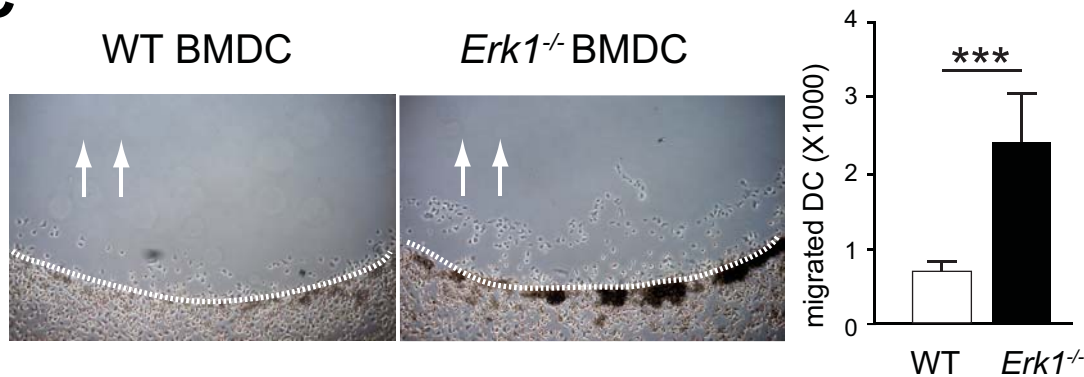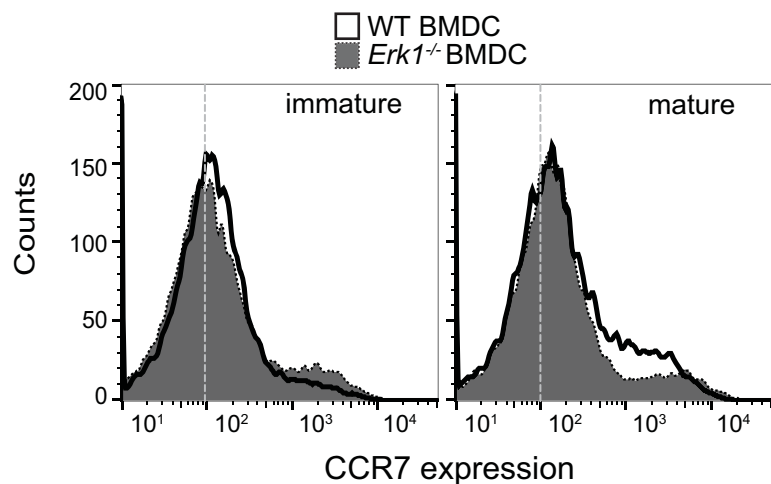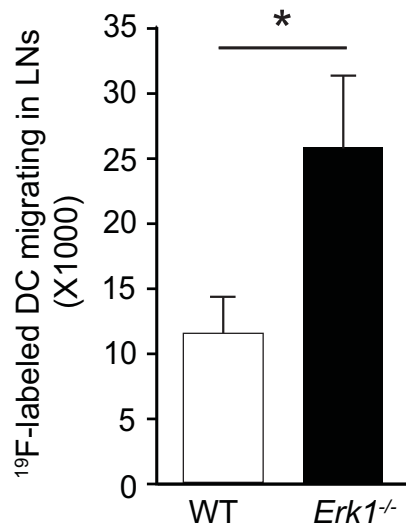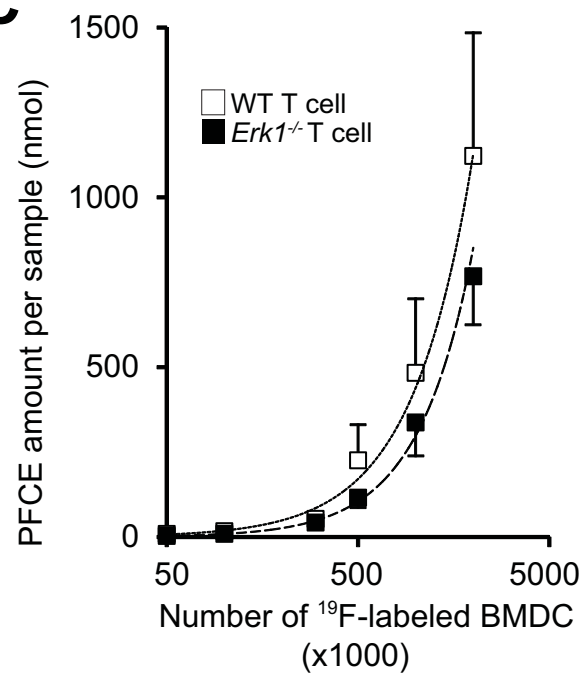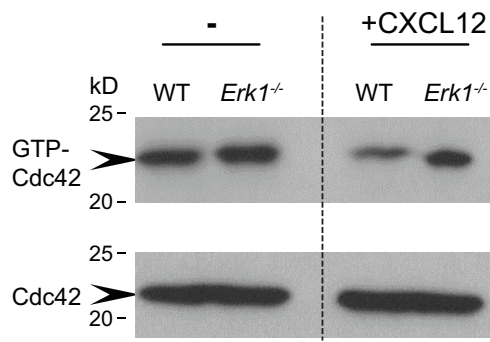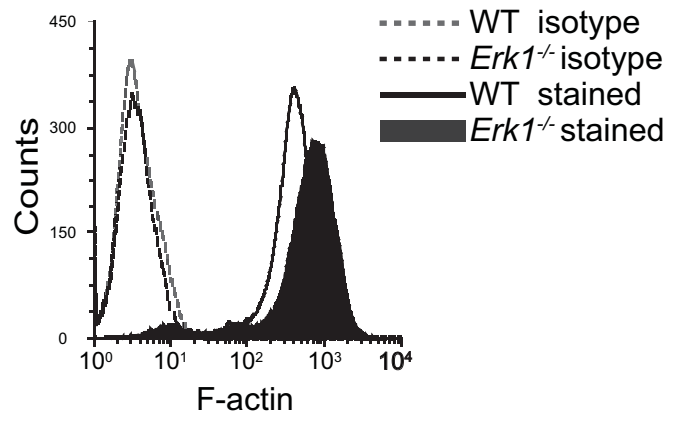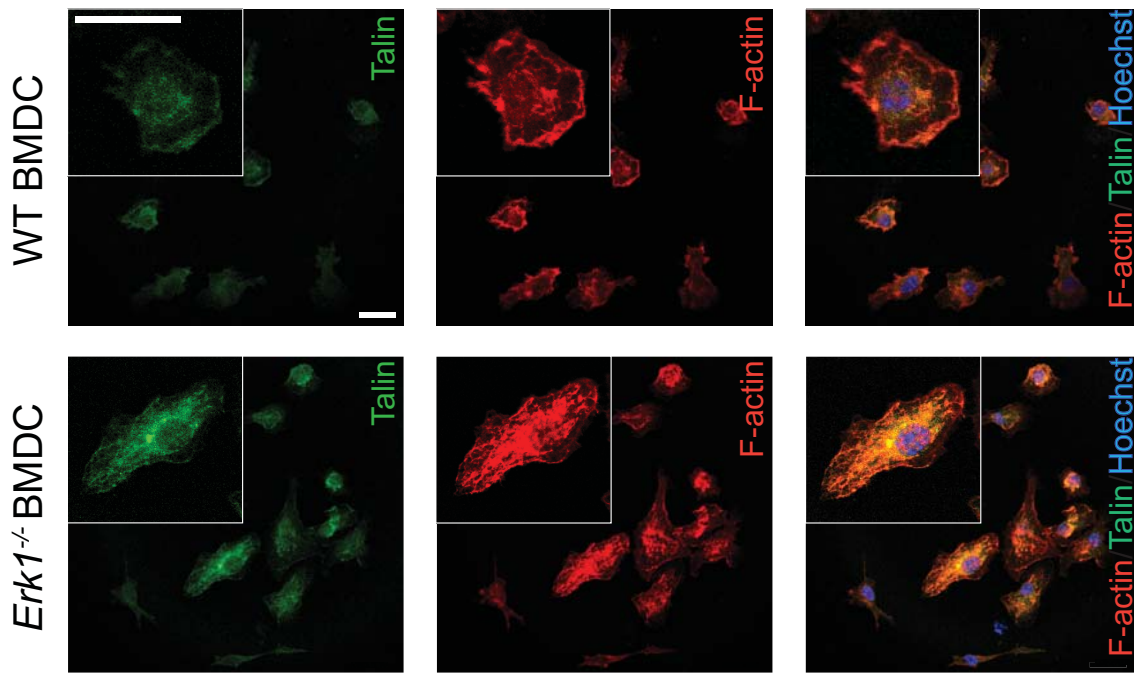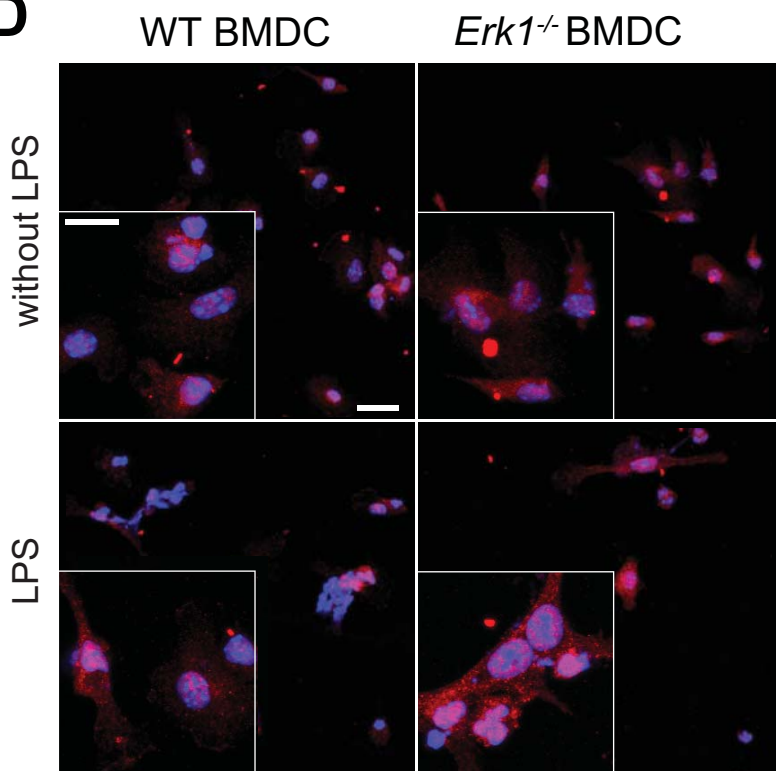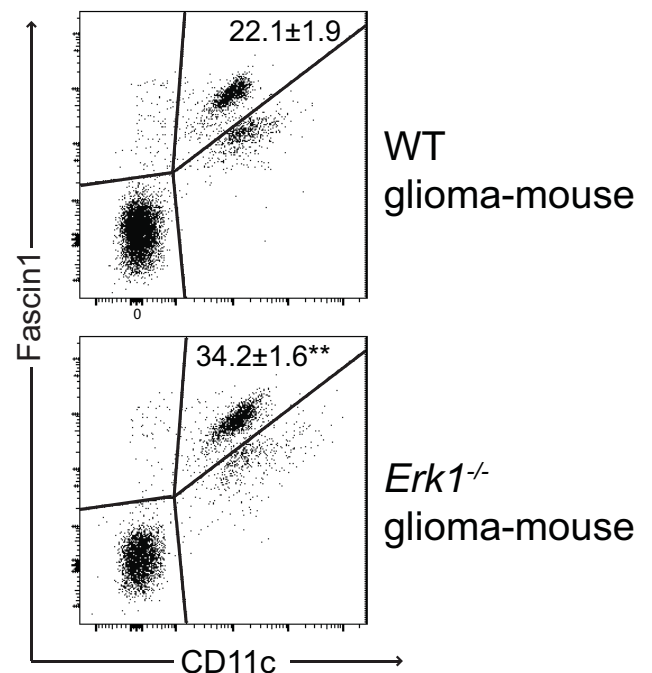
Figure 5

Figure 6

A
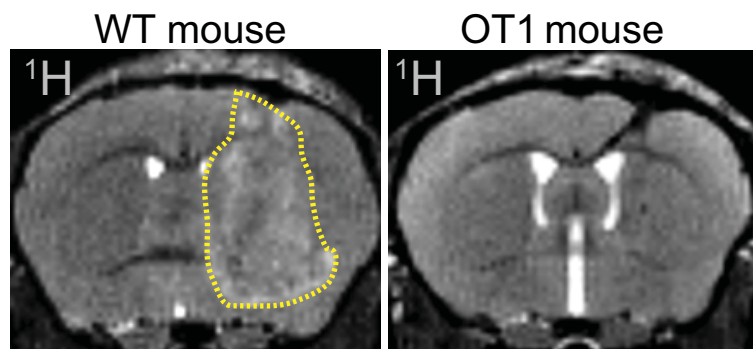
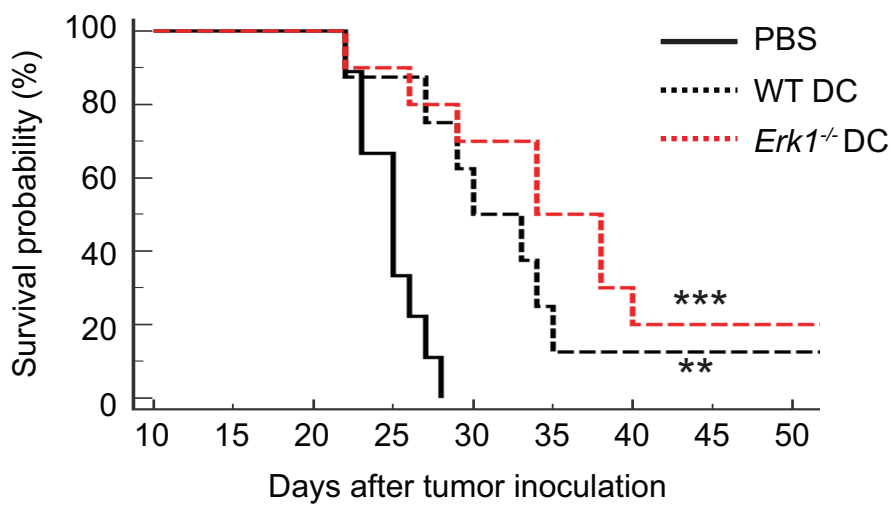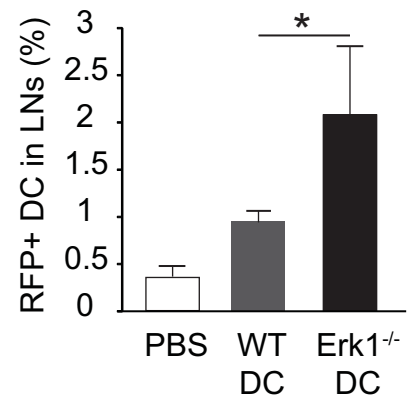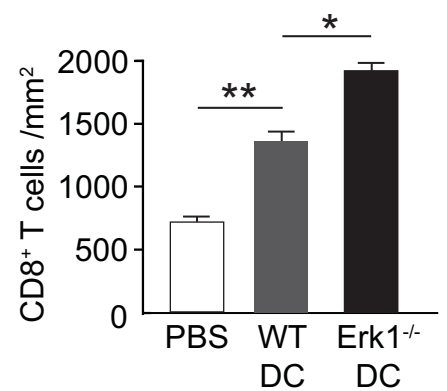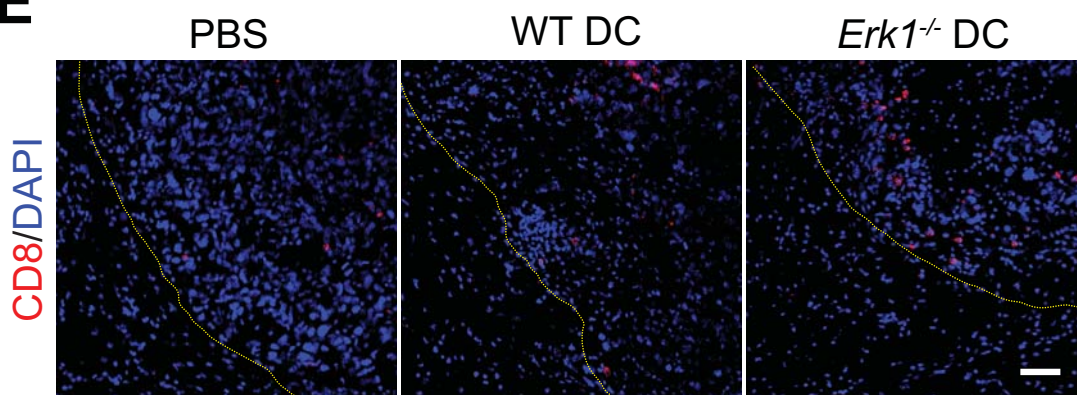| Glioma cell		Mouse	Tumor
WT-GL261	→	WT	yes
WT-GL261	→	OT1	yes
OVA-GL261	→	WT	yes
OVA-GL261	→	OT1	no

B
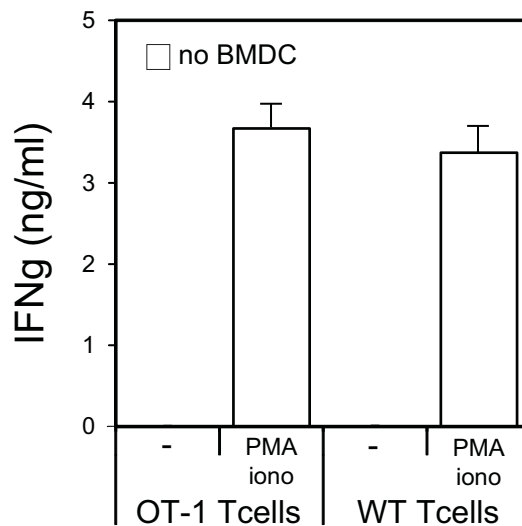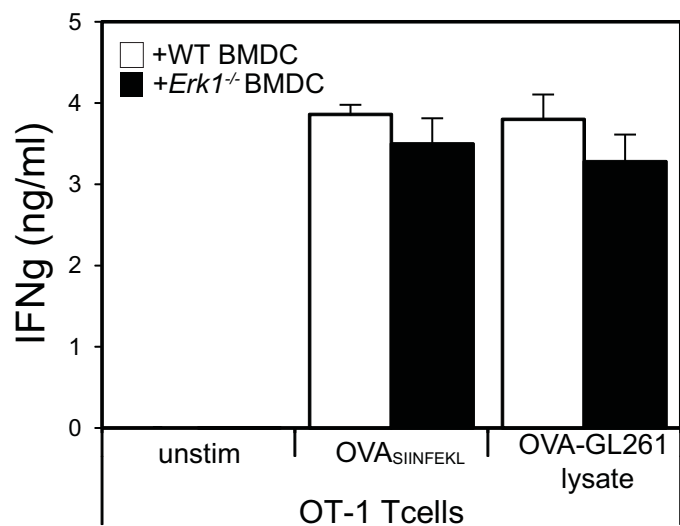
Figure 7

A
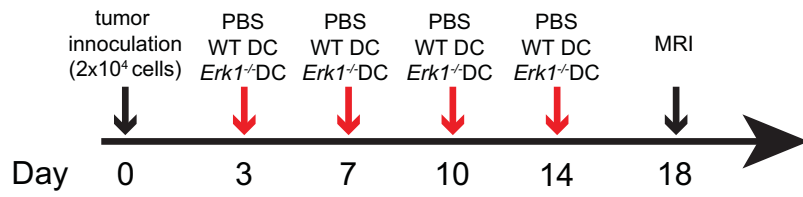
B
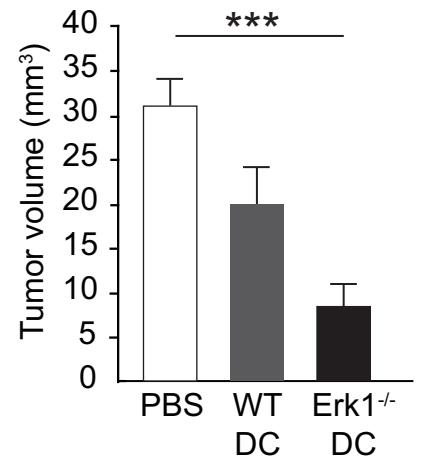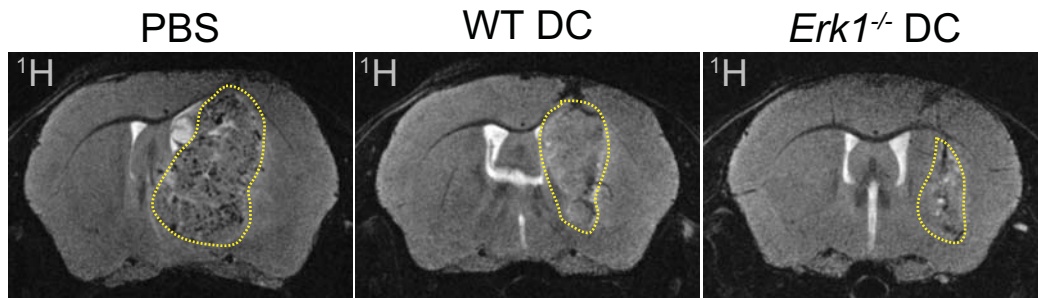
C

D

E

Supplementary Materials

SUPPLEMENTARY METHODS

Retroviral vectors and virus supernatant

Full-length OVA-sequence was amplified from pLOVASN via PCR using following primer-sequences: 5´-ATA<u>GTCGAC</u>CACCATGGGCTCCATCGGTG-3 (fwd) and 5´-ATA<u>GCGGCCGC</u>TTAAGGGGAAACACATCT-3 (rev). Underlined are the introduced restriction-sites for SalI and NotI. After digestion of the pMP71-IRES-GFP vector and the resulting amplicon with SalI and NotI restriction enzymes, both DNA-fragments were ligated using a Rapid DNA Ligation Kit (Roche). The resulting construct, pMP71-OVA-IRES-GFP, was verified by digestion with PstI restriction enzyme as well as DNA sequence analysis. Ecotropic viral vectors were produced using the Platinum-E packaging cell line (1). Viral supernatants were harvested 48 h following transfection, filtrated (0.45-μm pore size) and stored at -80 °C.

Transduction of GL261 cells and murine T cells

GL261 murine glioma cells (National Cancer Institute) were cultured at 37 °C and 5 % CO_2 in RPMI 1640 with 200 mM glutamine, 50 U/ml penicillin, 50 μg/ml streptomycin, and 10 % FBS (all from Invitrogen). GL261 cells (5×10^4) were seeded into 24-well plates and after 16 h, 1 ml viral supernatant supplemented with 4 μg/ml protamine sulfate (Sigma-Aldrich) was added prior to centrifugation for 1.5 h (800 g, 32 °C). After 24 h, the supernatant was exchanged with viral supernatant (2 ml) supplemented with protamine sulfate and 48 h later, the cells were analyzed by flow cytometry for expression of GFP and H2kb-SIINFEKL complexes. Transduction efficiency

reached 76% for MP71-OVA-IRES-GFP. To generate a 100 % GFP$^+$H2kb-OVA$^+$ cell population, these cells were bulk-sorted using a FACSARIA II (BD Biosciences).

To transduce murine primary splenocytes, 2×10^6 cells/ml were supplemented with 1 µg/ml anti-CD3 mAb, 0.1 µg/ml anti-CD28 mAb (BD Biosciences) and 10 IU IL-2 (Proleukin Novartis) and cultured overnight. The cell density 1×10^6 per ml were seeded in 24 well plates coated with 12.5 µg/ml RetroNectin (Takara) and supplemented with 4×10^5 beads/ml mouse T-Activator CD3/CD28 (Life Technologies), 10 IU/ml IL-2, 4 µg/ml protamine sulfate and virus-containing supernatant (MOI = 2). Following centrifugation for 1.5 h (800 g, 32 °C), the cells were incubated at 37 °C for 48 h. The medium was replenished with 10 ng/ml human recombinant IL-15 (Peprotech).

MRI methods

For *in vivo* MR measurements, mice were anesthetized shortly before and during the MR session using a mixture of isoflurane (Baxter) as inhalation narcosis (0.5 - 1.5%), pressurized air and oxygen. The core body temperature of the mice was maintained at 37 °C. Respiration rate and temperature were monitored using a remote monitoring system (Model 1025, SA Instruments Inc.).

In vivo assessment of glioma growth using ^1H MR microscopy. For comparing glioma tumor size in WT and *Erk1$^{-/-}$* glioma-bearing mice, mice brain were imaged on day 14 after the intracereberal inoculation of GL261 cells (14 dpi). For comparing glioma tumor size after vaccination, mice were imaged 18 dpi after the intracereberal inoculation of GL261 cells. Anesthetized mice were placed below a cryogenically-cooled quadrature radiofrequency (RF) coil (CryoProbe, Bruker Biospin) tailored for mice brain MR (2). T$_2$-weighted images (RARE,

repetition time (TR) = 3268 ms, echo time (TE) = 60 ms, RARE factor = 12, 8 averages) were acquired with the same slice geometry (FOV = (18×18) mm^2, matrix size = 350×350, slice thickness = 270 μm, in-plane spatial resolution = 51 μm, 21 coronal slices covering a brain region of 5.67 mm starting at the frontal end of the cerebral cortex (approx. Bregma 3.56 to -2.11 mm) (3). Tumor regions were manually segmented and the volume calculated in Fiji by adding up the voxel volumes.

Imaging inflammatory cell infiltration using in vivo $^1H/^{19}F$ MRI. For studying infiltration of immune cells from the peripheral circulation into glioma tissue, glioma-bearing mice were injected with rhodamine-tagged ^{19}F nanoparticles containing 80 μmol perfluoro-15-crown-5-ether (PFCE) 18 dpi via tail vein. After 18 h of injection, $^1H/^{19}F$ MRI was performed using an in-house built dual-tunable $^{19}F/^1H$ head coil (4) and a protocol consisting of a 3D RARE sequence with an isotropic resolution of 250 μm³ for ^{19}F (TR/TE = 800/5.9 ms, 128 averages) and of 125 μm³ for ^{1}H (TR/TE = 1500/47 ms) MRI. ^{19}F signal intensity was calculated in Fiji.

Visualizing in vivo BMDC migration using $^1H/^{19}F$ MRI. BMDC were incubated with ^{19}F nanoparticles (containing 20 μmol PFCE) and 1 μg/ml full-length chicken EndoGrade ovalbumin (endotoxin conc.<1 EU/mg; Hyglos). BMDC were further matured by 0.5 μg/ml lipopolysaccharide (LPS). Following overnight incubation, unbound ^{19}F nanoparticles were washed thoroughly from the culture with warm PBS. BMDC were then harvested and applied intradermally into hind limbs (one limb received 5×10^6 WT BMDC, the other received 5×10^6 *Erk1$^{-/-}$* BMDC) of WT mice and imaged 4 h after injection. Using a $^1H/^{19}F$ dual-tunable volume birdcage resonator (Rapid Biomed), gradient echo images were acquired using a 3D-FLASH sequence for ^{19}F (TR/TE = 8/3 ms; 80 averages, flip angle = 10°) and for ^{1}H (TR/TE = 11/4 ms; 8 averages, flip angle = 15°).

In vitro ^{19}F MR Spectroscopy (MRS). Following harvesting, BMDC (1×10^6) labeled with ^{19}F nanoparticles were fixed in 2 % paraformaldehyde (PFA) and transferred to NMR tubes (external diameter: 4.947 ± 0.019 mm; Wall thickness: 0.043 ± 0.02 mm; VWR International GmbH) and the uptake of ^{19}F nanoparticles monitored by ^{19}F spectroscopy. Different BMDC numbers were employed to achieve a ^{19}F signal to cell calibration. We employed an in-house built ^{19}F-tuned loop RF coil (5) for signal transmission and reception and a 90° block pulse with 10 kHz bandwidth for ^{19}F signal excitation. The amount of PFCE in each sample was calculated from the amplitude of the extrapolated monoexponential decay, at t=0 of the free induction decay (FID) ^{19}F MR signal, which is proportional to the ^{19}F concentration. A standard consisting of 500 mM PFCE was used as quantitative reference in all of these experiments. The same MRS method was employed to measure the ^{19}F signal in popliteal LNs extracted from mice following intradermal application of ^{19}F-labeled BMDC. The number of ^{19}F-labeled BMDC in each LN was quantified using the BMDC calibration curves. NMR data processing and analysis were performed in Matlab (R2010a, The MathWorks, Inc.).

References

1.   Morita S, Kojima T, Kitamura T. Plat-E: an efficient and stable system for transient packaging of retroviruses. Gene therapy. 2000;7:1063-6.

2.   Waiczies H, Millward JM, Lepore S, Infante-Duarte C, Pohlmann A, Niendorf T, et al. Identification of Cellular Infiltrates during Early Stages of Brain Inflammation with Magnetic Resonance Microscopy. PloS one. 2012;7:e32796.

3.   Franklin GPaKBJ. The Mouse Brain in Stereotaxic Coordinates, Third Edition. 3 ed: Academic Press; 2007.

4.   Waiczies H, Lepore S, Drechsler S, Qadri F, Purfurst B, Sydow K, et al. Visualizing brain inflammation with a shingled-leg radio-frequency head probe for 19F/1H MRI. Scientific reports. 2013;3:1280.

5.   Waiczies H, Lepore S, Janitzek N, Hagen U, Seifert F, Ittermann B, et al. Perfluorocarbon particle size influences magnetic resonance signal and immunological properties of dendritic cells. PloS one. 2011;6:e21981.